

Laser-Induced Colloidal Writing of Organometallic Precursor–Based Repeatable and Fast Pd–Ni Hydrogen Sensor

Guy Rahamim, Ehud Greenberg, Khalil Rajoua, Frédéric Favier, Hagay Shpaisman, David Zitoun

▶ **To cite this version:**

Guy Rahamim, Ehud Greenberg, Khalil Rajoua, Frédéric Favier, Hagay Shpaisman, et al.. Laser-Induced Colloidal Writing of Organometallic Precursor–Based Repeatable and Fast Pd–Ni Hydrogen Sensor. Advanced Materials Interfaces, 2019, 6 (19), pp.1900768. 10.1002/admi.201900768 . hal-02322237

HAL Id: hal-02322237
https://hal.science/hal-02322237

Submitted on 9 Dec 2020

HAL is a multi-disciplinary open access archive for the deposit and dissemination of scientific research documents, whether they are published or not. The documents may come from teaching and research institutions in France or abroad, or from public or private research centers.

L'archive ouverte pluridisciplinaire **HAL**, est destinée au dépôt et à la diffusion de documents scientifiques de niveau recherche, publiés ou non, émanant des établissements d'enseignement et de recherche français ou étrangers, des laboratoires publics ou privés.

Laser-Induced Colloidal Writing of Organometallic Precursor–Based Repeatable and Fast Pd–Ni Hydrogen Sensor

Guy Rahamim, Ehud Greenberg, Khalil Rajouâ, Frederic Favier, Hagay Shpaisman,* and David Zitoun*

G. Rahamim, E. Greenberg, Dr. H. Shpaisman, Prof. D. Zitoun
Department of Chemistry and Institute for Nanotechnology and Advanced Materials (BINA), Bar Ilan University, Ramat Gan 5290002, Israel
E-mail: hagay.shpaisman@biu.ac.il; david.zitoun@biu.ac.il
Dr. K. Rajouâ, Dr. F. Favier
Institut Charles Gerhardt Montpellier (ICGM), CNRS UMR 5253– Université de Montpellier, Montpellier, France

Abstract
The advent of hydrogen economy brings new challenges in terms of safety and sensing with a need for fast and low-cost monitoring of hydrogen concentration. Herein, a repeatable process for the fabrication of Pd-based hydrogen sensor is presented. First, a room-temperature reaction of organometallic precursors yields colloidal Pd/Ni alloyed nanoparticles. This organic solvent-based colloidal dispersion shows stability over months even with a relatively high metal content (≈1 wt %). Then, a laser induced microbubble deposits the nanoparticles in predetermined patterns from a microdroplet dispersion that is placed on a glass slide. An optical microscope monitors the writing process while a multimeter measures the sensor's conductance, assessing the success of the fabrication process. The fabricated sensors demonstrate excellent hydrogen detection performance in terms of response time, signal stability, and detection limit down to 100 ppm of H2 in air at room temperature.

1. Introduction

The high energy density of hydrogen makes it the most promising and cleanest technology to replace fossil fuels for transportation, besides the more established use of hydrogen in industry.[1–4] This high energy density comes with a downside in terms of safety, with low minimum ignition energy (0.017 mJ), high combustion heat (142 kJ g−1), wide flammability range (4–75%), and high permeability of hydrogen gas.[3] The transition toward hydrogen economy must include the deployment of hydrogen monitoring and hydrogen sensing which is not straightforward since it is a colorless, odorless, and tasteless flammable gas. There is an obvious need for fast and accurate sensing of H2 generation or accumulation to prevent explosions.

Among the diverse sensing techniques, resistive gas sensors display good performance and low cost. Palladium has been investigated as hydrogen sensor material due to its high dissociative absorption of hydrogen. When coupled with semiconductor material, the dissociate hydrogen might affect the semiconductor electron depletion layer resulting with sensing capabilities.[5–8]

During hydrogen absorption, the metallic phase experiences a crystallographic lattice expansion and a conductivity decrease, eventually converting to a semiconductor.[9,10] Charge pathways may also decrease due to cracks in the films after expansion.[11,12] The resistive response, as a function of hydrogen concentration, enables hydrogen sensing as reported in the literature.[13–17]

The volume expansion of Pd, upon hydrogen absorption, may lead to another phenomenon that could be used for sensing. In nanogranular systems the volume expansion results in closure of nanogaps and provides new electric pathways thus demonstrating a decrease in resistivity. This phenomenon happens mainly in thin films and nanogap Pd sensors, which show improved sensitivity and response time compared to bulk Pd sensors.[18–24] Quantum tunneling may also explain the response of nanogap systems, even when the hydrogen absorption does not fully close the gaps.[16] The main drawback of Pd for hydrogen sensing is the hysteresis effect caused by the expansion (mechanical deformation) of palladium hydride during its transition from α to β phase,

upon repeated exposure to hydrogen. The fabrication of very thin films partially overcomes this effect,[23,25,26] and the alloying of Pd, mainly with Ni, allows decreasing the hysteresis.[14,27,28]

Most of the research in this field during recent years have targeted the fabrication of thin films and/or alloyed Pd systems, using sputtering,[10–12,18,19,25,28–32] electron-beam evaporation,[9,14,21–23] and pulsed laser deposition[15] techniques. Alongside physical deposition techniques, wet chemical deposition methods, that are known to be low cost and versatile, can yield efficient sensors through electrodeposition[24,33] or colloidal deposition.[34] Colloidal synthesis represents the state-of-the-art in terms of control over all the parameters of nanoparticles (NPs) that could be used to construct the hydrogen sensors. Specifically, organometallic precursors yield NPs under mild conditions of temperature and pressure, giving rise to an accurate control on the kinetics of the NPs formation and growth.[35–37] Colloidal methods allow for the formation of composite materials which can be sprayed to form a thin film, like Pd nanocube–graphene, core–shell Pt/Pd–graphene hybrid sensors, [38,39] or Pd nanocube-MWCNTs.[40]

The electrophoretic deposition (EPD) method could be used for depositing NPs from a colloidal solution, and has been demonstrated for Pd on InP and GaN.[34,41,42] Other deposition methods rely on applying an electric,[43] magnetic, or acoustic field for the spatial control on the colloids.[44] Alas, these methods are not optimized for formation of on demand arbitrary controlled micropatterns.

Localized bottom-up on demand micropatterns could be formed by directing light to specific locations. A laser beam focused on a dispersion of NPs leads to the formation of a microbubble on the substrate due to heating of the solvent. Convective flows around the microbubble carries NPs to its base where some of them are pinned.[45] Moving the focused beam relative to the substrate results in material deposition along a predetermined path. This method is referred to as the laser induced microbubble technique (LIMBT). Lately Armon et al.[46] have shown that modulation of the laser significantly improves the control over the microbubble and the pinning of materials, and could be used for formation of continuous conductive micropatterns. Here we show for the first time how modulated-LIMBT is used to micropattern NPs for fabrication of hydrogen sensors.

Herein, we present a repeatable process for the fabrication of Pd-based hydrogen sensors. In the first step, the room-temperature reaction of organometallic Pd and Ni precursors yield a colloidal dispersion of Pd/Ni alloyed NPs. This organic solvent-based colloidal dispersion shows stability over months even with a relatively high metal content (≈1 wt%). Then, using modulated-LIMBT, Pd/Ni NPs are deposited from a microdroplet of the above colloidal dispersion. The NPs are selectively deposited along a predetermined path, thus bridging the gap between two gold pads on top of a glass substrate. The resistivity between the two gold pads changes as a function hydrogen concentration, and these sensors were tested in air at room temperature to assess the sensitivity and reaction time in a real environment.

2. Results and Discussion

The overall flowchart shown in Figure 1a displays the steps for sensor fabrication: organometallic-based synthesis of Pd–Ni colloids and laser-induced deposition. Figure 1b shows an illustration of the sensing bench-testing system.

2.1. PdNi Alloy Colloidal Synthesis and Characterization

The organometallic precursors easily decompose under hydrogen through the hydrogenation of the ligands and release of the metal centers (see Supporting Information). The reaction occurs at low temperature (35 °C) and in a short time (12 min) which enables the homogeneous nucleation of small NPs. The colloidal dispersions are stored without any further treatment or purification. The yield is close to 100% and the colloidal dispersion is stable for months. The metal weight concentration in the dispersion is set to 1 wt%, a relatively high value in the field of metal NPs dispersed in an organic solvent. The long chain alkylamines stabilize the colloidal dispersion for months and facilitate the ability for small particles size. Alkylamines are surfactants that can be easily displaced or removed for the fabrication of the sensors, in contrast to other surfactants which

strongly bind to the surface of Pd (for instance alkylthiols).

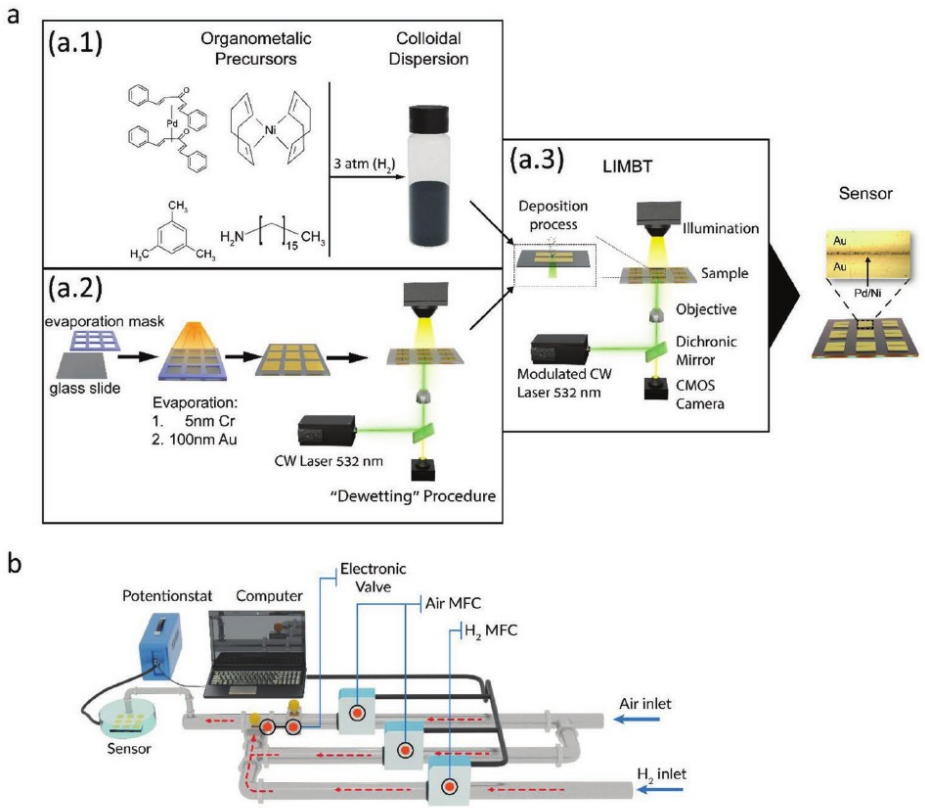


Figure 1. a) Overall fabrication pathway: a.1) organometallic-based NPs synthesis scheme; a.2) illustration of the conductive pads fabrication process; a.3) illustration of the deposition process of the synthesized NPs by using modulated-LIMBT. b) Scheme of the sensing bench-testing system.

The NPs are characterized by transmission electron microscopy (TEM) and high-resolution TEM (HRTEM), energy dispersive X-Ray spectroscopy (EDS), and X-ray diffraction (XRD) (Figure 2). The NPs are well dispersed and homogeneous in size (Figure 2a). The particle size dispersion (PSD) is derived from the analysis of 300 particles visualized by TEM, using the ImageJ software. The colloids display a lognormal PSD of 4.6 ± 1.4 nm. The EDS measurements (Figure 2c) on the NPs confirm the initial stoichiometry of the organometallic precursors with a metallic ratio of Pd0.9Ni0.1. The atomic plane spacing (0.222 nm) shown in Figure 2b is very close to pure Pd (0.223 nm), and indicates the formation of a Pd-rich alloy.

The XRD shows the presence of a single phase (Figure 2d). The lattice parameters are very close to face centered cubic (FCC) Pd (JCPDS # 05–0681; Fm-3m, a = 3.8902 Å: red lines) and do not show the presence of FCC Ni (JCPDS # 04–0850; Fm-3m, a = 3.5238 Å: blue lines). The two metals form an alloy, as expected from the bulk phase diagram. The very fast decomposition of the organometallic precursors can explain the very small particle size and the formation of a disordered statistical alloy.

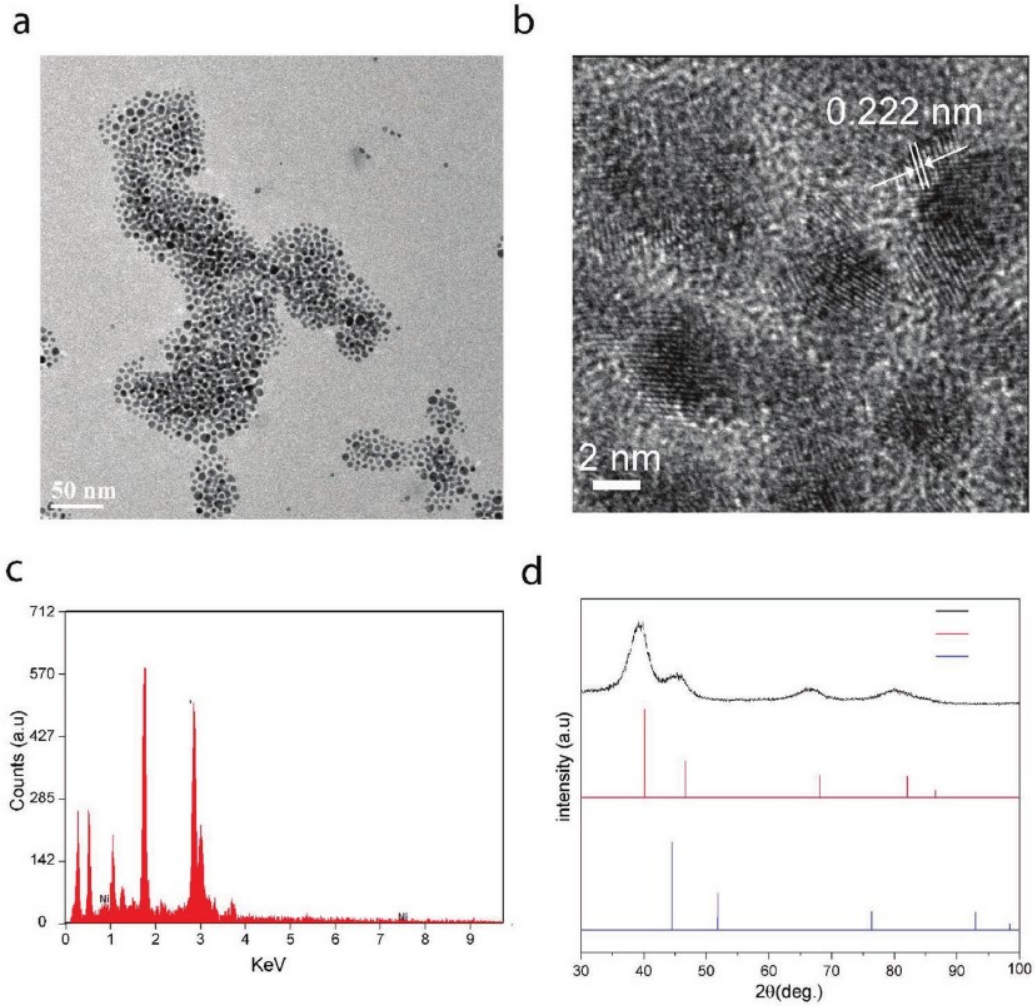


Figure 2. a) TEM and b) HRTEM images of the PdNi NPs; c) EDS spectrum and d) X-ray diffraction pattern of the PdNi NPs.

2.2. Modulated-LIMBT Deposition

First, two gold pads that serve as electrodes with a 3–4 μm gap between them (Figure S1A, Supporting Information) were formed by dividing a larger gold pad (Figure 1a.2) that was evaporated on a glass substrate. This is achieved by metal dewetting using a 532 nm laser. Then, a micro droplet (10 μL) of the colloidal dispersion is placed on the electrodes. We use modulated-LIMBT[46,47] in order to bridge the gap between the gold electrodes with the Pd0.9Ni0.1 NPs. The laser beam is focused at the liquid/substrate interface. The colloidal dispersion strongly absorbs the laser beam, causing local temperature increase of the solvent. The solvent's vapor pressure rises until a microbubble is formed. The temperature gradient between the top and bottom of the microbubble leads to formation of two types of convection flows: natural (due to the temperature/density gradient) and Gibbs−Marangoni (due to changes in surface tension). These two convection mechanisms lead to pinning of the NPs at the contact line between the microbubble and the substrate. The motorized stage is set so the deposition occurs along the gap between the electrodes (Figure 3a). The optimization of the LIMBT modulation parameters (power, stage velocity, and duty cycle) was determined by connecting the two Au pads to a multimeter and measuring the conductivity of the deposited material in real time until it reaches a measurable resistance. The resistance between the Au pads monitors the formation of conductive PdNi bridges in situ. The deposited layer was observed by a SEM (Figure 3a) and consists of nanoscale particles visualized by high resolution SEM (Figure 3b). This points at the successful assembly of a conductive layer directly from the Pd0.9Ni0.1 colloidal dispersion, without any further processing. Atomic force microscopy (AFM) gives the height profile of the deposited layer. Figure 3c shows a line-scan along the deposited layer. The average thickness was found to be 360 ± 160

nm. The inhomogeneity in the deposited thickness is due to the sequential deposition of overlapping rings (contact lines between the microbubble and the substrate) that is sometimes observed in deposits of LIMBT. The modulated-LIBMT assisted colloidal fabrication protocol yields sensing layers with a broad range of initial resistivity. The sensors' activation is carried out through exposure to hydrogen[21,24,48] that results in a high increase of the sensors' initial resistance.

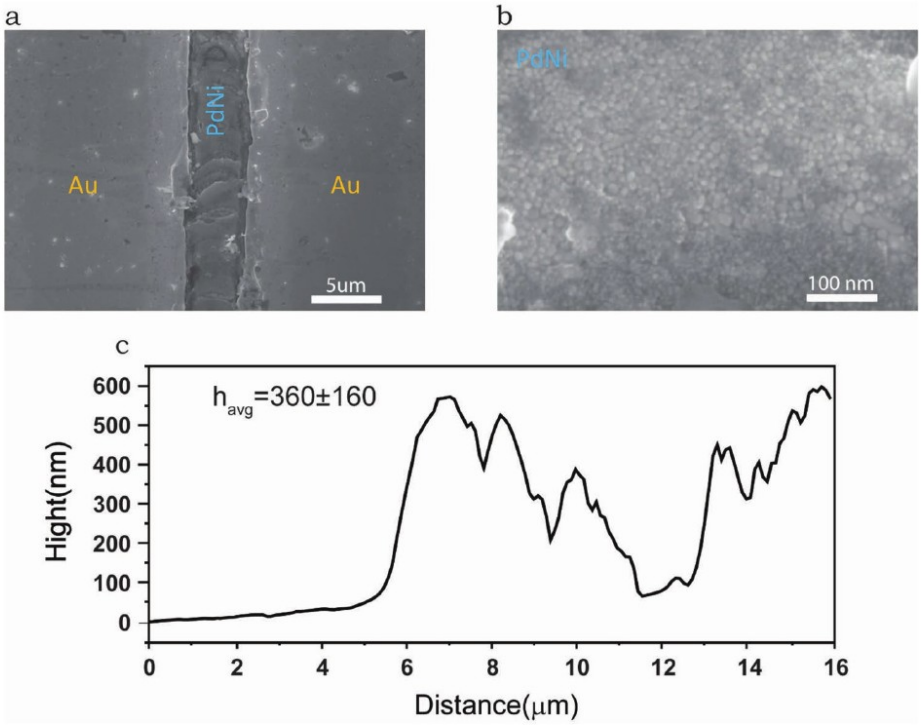


Figure 3. a) SEM image of the colloidal deposition between the two electrodes. b) High resolution SEM micrograph of the deposited PdNi showing the active material surface. c) AFM line-scan of the deposited layer.

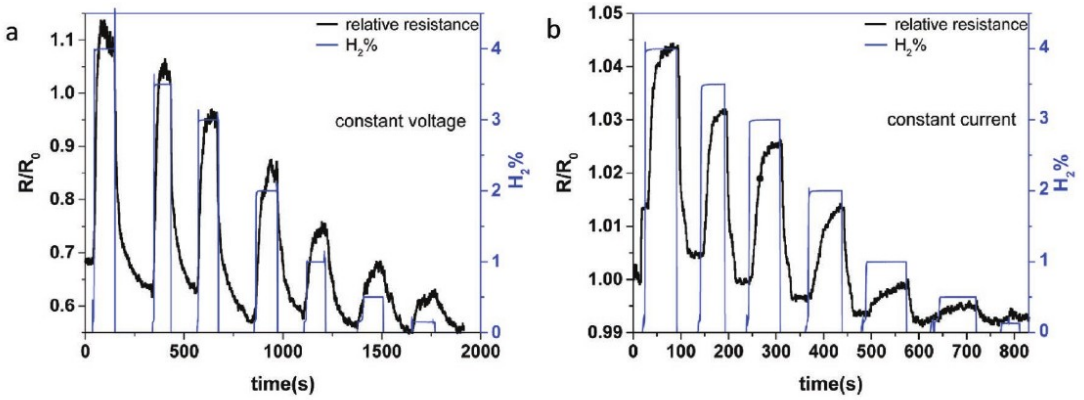


Figure 4. Fabricated sensor response to varying H_2 concentrations (4–0.15%) at a) constant voltage and b) constant current modes. The sensor shows a quasi-linear electrical response to hydrogen at room temperature.

2.3. Sensing Performances

The sensors were tested in a homemade testing chamber connected to a gas channels system equipped with mass-flow controllers and electrical valves, with an interface to Labview software for automated measurements (Figure 1b). The Au pads were connected with Cu wires and silver paste to a potentiostat. In general, sensors with different morphological and electrical properties require optimization of the working mode (constant current or constant voltage) and a specific set of electrical input parameters. For both working modes the operation voltage and current tuning was initiated at low values and slowly increased in order to achieve maximal response to H2 while preventing Joule heating effects that might result in the sensor's failure. The optimal electrical parameters for the sensor's measurements shown in Figure 4 were set to 7 V for

the constant voltage mode and 0.11 mA for the constant current mode. The H2 concentrations in air varied from 4% (the lower limit for explosion in air[2,14,24]) down to 0.15%. The electrical signals obtained were monitored and recorded. The analysis of the results reveals that the response time does not vary with the operation mode. However, the constant voltage mode shows an improved response amplitude with sharpened signals and lower detection limit (Figure 4) when compared with the constant current mode. Therefore, below we report the sensing response using the constant voltage mode, unless stated otherwise.

After finding the optimal operation mode, we measured the sensors' response to lower concentrations, in the range of 0.5–0.01% of H2 with a 0.5 V operation bias. The ability to detect lower concentrations than the explosion limit (4% H2) is crucial for safety and is required in all hazard alarms. The results presented in Figure 5a indicate stable and sharp signals obtained while exposing the sensor to low H2 concentrations. While exposed to concentrations above 0.1% H2, the sensor signal displays a slight drift. Exposing to lower concentrations than 0.1% reveal a more stable baseline with longer response/recovery times. Moreover, the sensor's response to 0.01% (100 ppm) of H2 displays a high and sharp amplitude, which might indicate the sensor ability to detect even lower H2 concentration. To test the stability of the signal, the sensor was repeatedly exposed to the edges of the selected concentration range. The sensor's signal for repeated exposure to 0.5% (Figure 5b) and 100 ppm (Figure 5c) H2 does not show a significant drift. The sensor's response is consistent, repeatable, and stable.

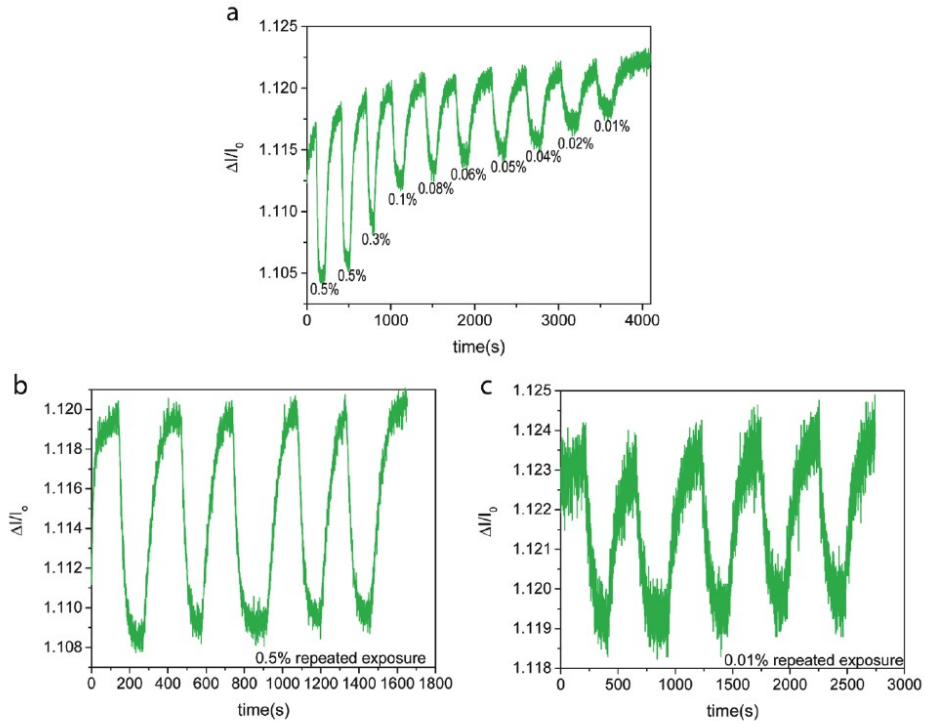


Figure 5. a) Sensor response to H_2 concentration between 0.5% and 0.01%. Stability tests of the response to b) 0.5% and c) 0.01% of H_2. All measurements were performed at constant voltage mode with a 0.5 V bias.

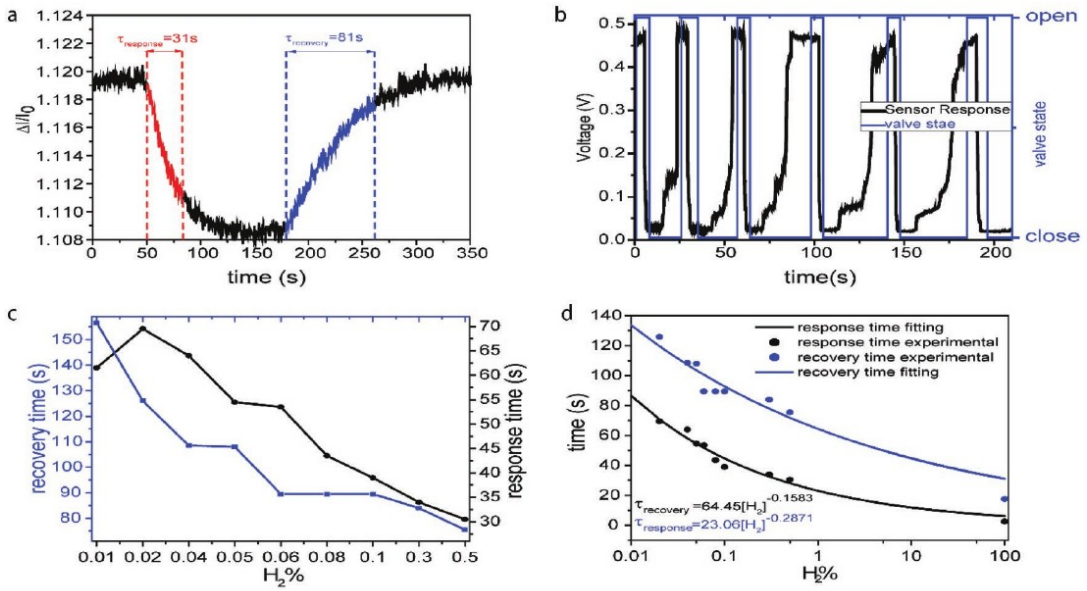


Figure 6. a) Response and recovery time for exposure to 0.5% H_2. b) Response time measurements for exposure to 100% of H_2. c) Response and recovery time as a function of H_2 concentration and d) fitting of the sensor's response and recovery time.

2.4. Response and Recovery Time Measurements

The response time is defined as the time needed for the sensor to reach 90% of the maximal signal amplitude, while the recovery time is the time needed for the signal to return within 10% from the base line. The layer of NPs is expected to show short response and recovery times due to its high surface area. We calculated the response/recovery times for each concentration tested. Figure 6a shows the response and recovery times for the exposure of the sensor to 0.5% of H2 . The results shown in Figure 6c reveal an inversely proportional behavior to the H2 concentration with a maximum response time of 69 s at 200 ppm followed by a slight decrease at 100 ppm. 0.5% H2 is detected within 31 s and higher H2 concentrations are expected to result in even faster response times. The recovery time shows a similar behavior with a maximum of 156 s for 100 ppm of H2 and a minimal recovery time of 75 s for 0.5% H2 .

We modified our testing system in order to measure shorter response and recovery times. Two electric valves were added very close to the testing chamber inlet, one for air flow and one for H2.

Both valves were computer controlled and interfaced with Labview. This modification was crucial to avoid any unwanted source of error, arising primarily due to the mass-flow controller (MFC) response/stabilization time and leakage.

The addition of the electrical valves allowed us to minimize the gas channel lengths and reach a low measurable gas channel volume. In this configuration, the gas channel volume was 2.5 cc and the flow 100 cc/min. These values were used to calculate the delay time that was found to be 1.5 s and was taken into account when determining short response times. At high H2 concentrations, the constant current operation mode provides faster responses. The current setpoint was 0.1 mA and the measurements were carried out with repeating exposure/washing of H2/Air. Figure 6b presents the response time measurements with different flow rates and 100% H2 and air cycling. The first three H2 exposures were at 100 cc/min followed by three H2 exposures at 50 cc/min. This allows us to study effect of flow rate on the sensor's response time.

The results are consistent with a response time of 2.5 ± 0.7s, for 100% H2. Power fitting of the low H2 concentration response times predict very well the high H2 concentration value (Figure 6d). Moreover, it was found there is no significant influence of the flow rate. However, the recovery time increases almost linearly with the flow rate. While the recovery times were in the range of 14–21 s for the 100 cc/min flow, the recovery times were in the range of 34–37 for the lower flow rate. Selected results from the literature can be found in Table S1 and Figure S2 in the Supporting Information.

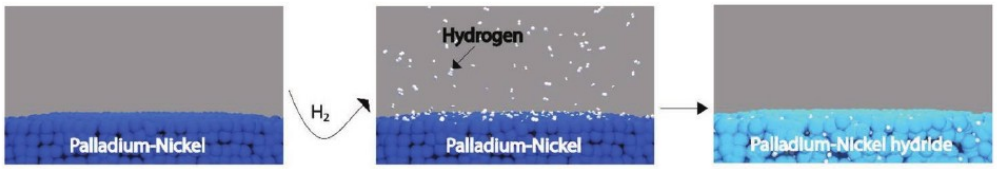


Figure 7. Sensing mechanism. Exposing the alloy to H_2 convert it into an alloy-hydride resulting with an increase of the overall resistance.

2.5. Sensing Mechanism

There are several sensing mechanisms associated with Pd-based sensors. Two of them can be related to the sensing response observed in this work. Exposing the sensor to H2 leads to the dissociation and absorption of the gas inside the NPs, resulting with two main changes that affect the device's resistance: formation of palladium hydride phase coupled with volume expansion. On one hand, palladium hydride has higher resistance compared with pure Pd, thus, the formation of hydride includes the increase of the device resistance. On the other hand, when working with nanostructures device (like our sensor), volume expansion of the NPs might induce higher contact between neighboring NPs, increasing the electrical percolation in the device, resulting with a conductive response. In our case, the increasing resistance (decreasing current) during exposure to H2 (Figures 4 and 5) points at major role of the first mechanism, hydride formation. The proposed mechanism is illustrated in Figure 7.

3. Conclusion

Herein, we have reported a novel sensor fabrication approach, combining an organometallic-based NPs synthesis followed by modulated-LIMBT deposition. The synthesis is fast and with high yield and the formed colloidal dispersions are stable for months. The modulated-LIMBT deposits the PdNi Nps between two gold pads, thus providing conductive functional sensors. The effective deposition method allows formation of hundreds of sensors even with the small-scale synthesis described. The sensors display excellent sensitivity to a wide range of H2 concentrations with a detection limit below 100 ppm.

Supporting Information

Supporting Information is available from the Wiley Online Library or from the author.

Acknowledgements

The authors thank Michael Mirilashvili for the fruitful discussions on the sensing mechanism.

Conflict of Interest

The authors declare no conflict of interest.

Keywords

hydrogen, laser deposition, nanoparticles, organometallics, sensors

References

[1] W. J. Buttner, M. B. Post, R. Burgess, C. Rivkin, Int. J. Hydrogen Energy 2011, 36, 2462.
[2] C. H. Han, D. U. Hong, J. Gwak, S. Do Han, Korean J. Chem. Eng. 2007, 24, 927.
[3] T. Hübert, L. Boon-Brett, G. Black, U. Banach, Sens. Actuators, B. 2011, 157, 329.
[4] C. Schwandt, D. J. Fray, Ionics 2000, 6, 222.
[5] M. Weber, J. Y. Kim, J. H. Lee, J. H. Kim, I. Iatsunskyi, E. Coy, P. Miele, M. Bechelany, S. S. Kim, J. Mater. Chem. A 2019, 7, 8107.
[6] A. Kumar, A. Sanger, A. Kumar, R. Chandra, RSC Adv. 2017, 7, 39666.

[7] A. Kumar, A. Kumar, R. Chandra, Sens. Actuators, B. 2018, 264, 10.
[8] M. Weber, J. H. Kim, J. H. Lee, J. Y. Kim, I. Iatsunskyi, E. Coy, M. Drobek, A. Julbe, M. Bechelany, S. S. Kim, ACS Appl. Mater. Interfaces 2018, 10, 34765.
[9] T. Xu, M. P. Zach, Z. L. Xiao, D. Rosenmann, U. Welp, W. K. Kwok, G. W. Crabtree, Appl. Phys. Lett. 2005, 86, 1.
[10] M. Ramanathan, G. Skudlarek, H. H. Wang, S. B. Darling, Nanotechnology 2010, 21, 125501.
[11] B. Wang, Y. Zhu, Y. Chen, H. Song, P. Huang, D. V. Dao, Mater. Chem. Phys. 2017, 194, 231.
[12] E. Lee, J. Lee, J. S. Noh, W. Kim, T. Lee, S. Maeng, W. Lee, Int. J. Hydrogen Energy 2012, 37, 14702.
[13] F. Yang, D. K. Taggart, R. M. Penner, Nano Lett. 2009, 9, 2177.
[14] M. Wang, Y. Feng, Sens. Actuators, B 2007, 123, 101.
[15] M. K. Kumar, M. S. R. Rao, S. Ramaprabhu, J. Phys. D: Appl. Phys. 2006, 39, 2791.
[16] J. Van Lith, A. Lassesson, S. A. Brown, M. Schulze, J. G. Partridge, A. Ayesh, Appl. Phys. Lett. 2007, 91, 181910.
[17] R. K. Joshi, S. Krishnan, M. Yoshimura, A. Kumar, Nanoscale Res. Lett. 2009, 4, 1191.
[18] M. Zhao, M. H. Wong, C. W. Ong, Appl. Phys. Lett. 2015, 107, 033108.
[19] J. Lee, W. Shim, E. Lee, J. S. Noh, W. Lee, Angew. Chem., Int. Ed. 2011, 50, 5301.
[20] J. Lee, W. Shim, J.-S. Noh, W. Lee, ChemPhysChem 2012, 13, 1395.
[21] T. Kiefer, F. Favier, O. Vazquez-Mena, G. Villanueva, J. Brugger, Nanotechnology 2008, 19, 125502.
[22] T. Kiefer, L. G. Villanueva, F. Fargier, F. Favier, J. Brugger, Nanotechnology 2010, 21, 505501.
[23] T. Kiefer, L. G. Villanueva, F. Fargier, F. Favier, J. Brugger, Appl. Phys. Lett. 2010, 97, 121911.
[24] E. C. Walter, F. Favier, R. M. Penner, Anal. Chem. 2002, 74, 1546.
[25] E. Lee, J. M. Lee, J. H. Koo, W. Lee, T. Lee, Int. J. Hydrogen Energy 2010, 35, 6984.
[26] K. J. Jeon, J. M. Lee, E. Lee, W. Lee, Nanotechnology 2009, 20, 135502.
[27] E. Lee, J. M. Lee, E. Lee, J. S. Noh, J. H. Joe, B. Jung, W. Lee, Thin Solid Films 2010, 519, 880.
[28] L. Sun, M. Chen, X. Peng, B. Xie, M. Han, Int. J. Hydrogen Energy 2016, 41, 1341.
[29] A. I. Ayesh, J. Alloys Compd. 2016, 689, 1.
[30] Q. Zhao, J. Shao, H. Tian, X. Li, C. Wang, J. Liu, Sens. Actuators, B 2018, 270, 475.
[31] X. Peng, H. Zhang, L. Sun, F. Liu, MATEC Web Conf. 2015, 26, 02003.
[32] X. Q. Zeng, M. L. Latimer, Z. L. Xiao, S. Panuganti, U. Welp, W. K. Kwok, T. Xu, Nano Lett. 2011, 11, 262.
[33] T. K. Kyun, J. S. Sang, M. C. Sung, IEEE Sens. J. 2006, 6, 509.
[34] K. Zdansky, R. Yatskiv, Sens. Actuators, B 2012, 165, 104.
[35] M. Shviro, D. Zitoun, Nanoscale 2012, 4, 762.
[36] M. Shviro, D. Zitoun, RSC Adv. 2013, 3, 1380.
[37] M. Shviro, S. Polani, R. E. Dunin-Borkowski, D. Zitoun, Adv. Mater. Interfaces 2018, 5, 1701666.
[38] D. Phan, G. Chung, Sens. Actuators, B 2014, 199, 354.
[39] D. Phan, A. S. M. I. Uddin, G. Chung, Sens. Actuators, B 2015, 220, 962.
[40] U. Yaqoob, A. S. M. I. Uddin, G. Chung, Sens. Actuators, B 2016, 229, 355.
[41] K. Zdansky, R. Yatskiv, O. Cernohorsky, K. Piksova, Key Eng. Mater. 2012, 507, 169.
[42] K. Zdansky, Nanoscale Res. Lett. 2011, 6, 490.
[43] R. Soheilian, H. Abdi, C. E. Maloney, R. M. Erb, J. Colloid Interface Sci. 2018, 513, 400.
[44] H. Sazan, S. Piperno, M. Layani, S. Magdassi, H. Shpaisman, J. Colloid Interface Sci. 2019, 536, 701.
[45] Y. Zheng, H. Liu, Y. Wang, C. Zhu, S. Wang, J. Cao, S. Zhu, Lab Chip 2011, 11, 3816.
[46] N. Armon, E. Greenberg, M. Layani, Y. S. Rosen, S. Magdassi, H. Shpaisman, ACS Appl. Mater. Interfaces 2017, 9, 44214.

[47] E. Greenberg, N. Armon, O. Kapon, M. Ben-ishai, H. Shpaisman, Adv. Mater. Interfaces 2019, 6, 1900541.
[48] F. Favier, E. C. Walter, M. P. Zach, T. Benter, R. M. Penner, Science 2001, 293, 2227.